Reduction of electron-phonon coupling in warm dense iron

A. Fernandez-Pañella [1,*] T. Ogitsu,[1] K. Engelhorn,[2] A. A. Correa,[1] B. Barbrel [3] S. Hamel,[1] D. G. Prendergast,[4]
D. Pemmaraju [4] M. A. Beckwith,[1] L. J. Bae [5] J. W. Lee [5] B. I. Cho,[5] P. A. Heimann,[6] R. W. Falcone,[3] and Y. Ping[1]

[1]*Lawrence Livermore National Laboratory, Livermore, California 94550, USA*
[2]*Advanced Light Source, Lawrence Berkeley National Laboratory, Berkeley, California 94720, USA*
[3]*Department of Physics, UC Berkeley, Berkeley, California 94720, USA*
[4]*The Molecular Foundry, Lawrence Berkeley National Laboratory, Berkeley, California 94720, USA*
[5]*Department of Physics and Photon Science, Gwangju Institute of Science and Technology, Gwangju, Korea*
[6]*Linac Coherent Light Source, SLAC National Accelerator Laboratory, Menlo Park, California 94025, USA*

The electron-ion relaxation dynamics in warm dense iron were investigated by time-resolved x-ray absorption near-edge spectroscopy (XANES). A novel analysis, combining *ab initio* density functional theory (DFT) and two temperature model (TTM) simulations, was developed to calculate the x-ray absorption spectra as a function of delay time. Here we present experimental evidence of changes at the XAS *L*3 edge of iron that are consistent with the reduction of the electron-phonon coupling under warm dense matter conditions. The experimental results are in agreement with the model that takes both the electron (T_e) and the ion temperature (T_i) dependence of the thermophysical properties into consideration, while models where either constant electron-phonon coupling factor (G) or only T_e-dependent G are used do not agree with the observed relaxation dynamics of iron.

I. INTRODUCTION

Femtosecond laser heating is a fast-growing and versatile technique to study the physical properties of matter in highly nonequilibrium or transient conditions between electrons and ions, i.e., each has a well-defined thermodynamic state but nonequal temperatures. At high enough laser intensities, warm dense matter (WDM) states can be created, which are defined by temperatures ranging $\sim 10^4$–10^5 K (~ 1–10 eV) and near solid densities [1]. This regime bridges the gap between condensed matter and plasma physics. Improving our understanding of the fundamental properties of matter in this complex regime is relevant for a large variety of fields like plasma physics [2], planetary science [3], inertial confinement fusion [4], laser ablation, and micromachining applications [5].

During the irradiation of a metal by an intense femtosecond optical pulse the electrons near the Fermi level undergo intensive photoexcitation, while the lattice remains cold. This highly nonequilibrium system offers a great opportunity to study the electron-ion relaxation dynamics in WDM conditions, which is realized in a picosecond time scale. Beyond the equilibration time scale the system will exhibit hydrodynamic expansion and becomes a dilute plasma. The focus of our work lies within the first few picoseconds where the system stays at near-solid density and in nonequilibrium conditions. Several experimental and theoretical studies on metals like aluminum [6], gold [7–13], and copper [14,15] have revealed

that the temperature dependence of the main thermophysical properties, such as the electron-phonon coupling factor (G) and the electron specific heat (C_e), is very sensitive to the details of the electronic density of states (DOS) of the material. The rate of energy transfer between the electrons and phonons can be expressed, in a simplified expression, as $\partial E_e/\partial t|_{e-ph} \sim G(T_i - T_e)$, where G is the electron-phonon coupling factor, and T_i, T_e are the ion and electron temperatures, respectively. It was reported that the G value of copper rises sharply from $G_{\text{Cu}} \sim 1 \times 10^{17}$ W m^{-3} K^{-1} at ambient conditions [16] to 4.5×10^{17} W m^{-3} K^{-1} at $T_e > 10^4$ K [14,15]. A similar trend was observed for gold [7]. These experimental results are consistent with the predictions based on first-principles electronic structure calculations by Lin *et al.* where the electron temperature dependence of the electronic DOS for an ideal lattice at $T_i = 0$ K was investigated. For noble metals, the Fermi level lies about 2–3 eV above the fully occupied *d* bands. The enhanced value observed in G, for $T_e > 10^4$ K, is due to an increased number of transition channels via excited hole states in *d* levels that now can make a substantial contribution to the thermophysical properties of the material. In contrast, the G temperature dependence for transition metals like iron is expected to be the opposite. Now, the Fermi level cuts through the high-energy edge of the *d* bands, generating a large density of electrons at the Fermi level that can easily be excited to lower density *s*-band states when the electron temperature rises. Lin's calculations have predicted that the large G value at room temperature, $G_{\text{Fe}} \sim 55 \times 10^{17}$ W m^{-3} K^{-1} [6], strongly decreases at WDM conditions by a factor of 4 at 20 000 K [see Fig. 3(a)].

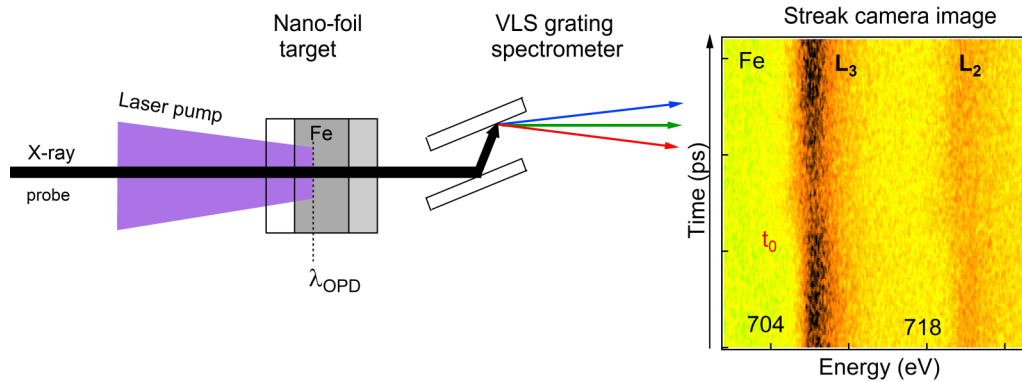*Corresponding author: ping2@llnl.gov

FIG. 1. Scheme of the experimental laser-pump x-ray-probe setup used at the Advanced Light Source at beamline 6.0.2. The raw streaked image is the average of 100 shots at a $F = 0.95 \, \text{J cm}^{-2}$. The arrival of the laser pulse is indicated by t_0. λ_{OPD} represents the optical penetration depth.

Here we present a detailed study of the thermophysical properties of warm dense iron upon femtosecond laser excitation probed by time-resolved XANES. We describe a novel analysis that explicitly considers the spatial temperature distribution of the electron and ion temperature within the target, as the experiments were performed under nonhomogeneous heating conditions.

First-principle density functional theory-molecular dynamic (DFT-MD) calculations were performed to calculate the electron temperature dependence of C_e, G, and K_e, the thermal conductivity, at several ion temperatures at both solid and liquid phases. One-dimensional two-temperature (TTM) simulations combined with *ab initio* derived dipole-matrix elements calculations were performed to obtain the theoretical XANES spectra. The details of the model, approximations, and DFT calculations used in this work are found in Ogitsu *et al.* [17]. We report experimental evidence of the reduction of the electron-phonon coupling in a transition metal at WDM conditions, an order of magnitude lower with respect to condensed matter conditions. While further investigation is needed to explore the apparent good agreement we observe between the experimental results and the calculations, this work also indicates that the thermophysical properties of iron, especially the electron-phonon coupling factor, depends significantly on the ion temperature and, at WDM conditions, it is crucial to take its effect into consideration to describe the equilibration dynamics between electrons and the ions. Furthermore, our results suggest that the Wang's formula [7], widely used at condensed matter conditions, is still valid up to the temperature range explored in our experiments, a few electron volts.

II. EXPERIMENTAL RESULTS

A. Experimental setup

The experiments were performed at the beamline 6.0.2 of the Advanced Light Source synchrotron facility using a laser-pump-x-ray-probe setup as shown in Fig. 1. The target was a polycrystalline 60-nm-thick iron foil coated on each side with a 40-nm-thick layer of silicon dioxide (front) and amorphous carbon (aC) (back). The tamping layers confined the foil, allowing us to observe the equilibration dynamics of iron at

a nearly constant solid density, and they also prevented its oxidation. A 150-fs (FWHM) Ti:sapphire laser pulse was split into three beams. The beam used as the pump was frequency doubled and focused onto the target with a spot diameter of 200 μm (FWHM). The streak camera was triggered by a second beam while the third one was frequency tripled and split to generate two UV timing fiducials. The experiments were performed above the damage threshold, at laser fluencies near 1 J cm^{-2}. After each laser shot the target was translated to a new undamaged location. The spectra shown in Fig. 1 is the average of 100 shots. Optical reflectometry and transmission measurements were performed at similar fluences to determine the laser absorption of SiO$_2$ and Fe at 400 nm, which were 15% and 40%, respectively. The fluences used in this work were sufficient to generate optical damage to the tamping layer in SiO$_2$. We measured the O K edge during the experiments and observed the onset of spectral changes (e.g., appearance of a small peak below the band gap, absorption within the band gap, broadening of the edge) in the XANES spectrum over time that are consistent with the ones described in [18]. These spectral changes of the heated SiO$_2$ indicate changes in its electronic structure with respect to the room temperature insulator solid. In Ogitsu *et al.* it was assumed that the net energy transport from iron to SiO$_2$ (or vice versa) via hot electrons created in these subsystems is negligible and the presence of the SiO$_2$ tamping layer was neglected in the TTM simulations [17]. The target thickness used in this work was 60 nm in order to have enough contrast at the Fe L_3 edge but it was larger than the optical penetration depth of iron, $\lambda_{\text{OPD}} = 12$ nm at 400 nm [19,20]. In d-band transition metals ballistic transport is not significant as it is in s/p-band metals like Au, due to a stronger electron-phonon coupling at room temperature that diminishes the energy transport to the depth of the material [8]. Thus, a temperature gradient was generated between the skin depth and the rest of the Fe sample. In contrast, homogeneous heating conditions in noble metals like Cu [8] or Au [8,21] are more readily achieved as the ballistic transport is larger than the λ_{OPD}, about 70–100 nm.

XANES is a powerful spectroscopic tool that probes the local geometry and the unoccupied DOS near the Fermi surface. XANES spectra were measured at the Fe L_3 edges
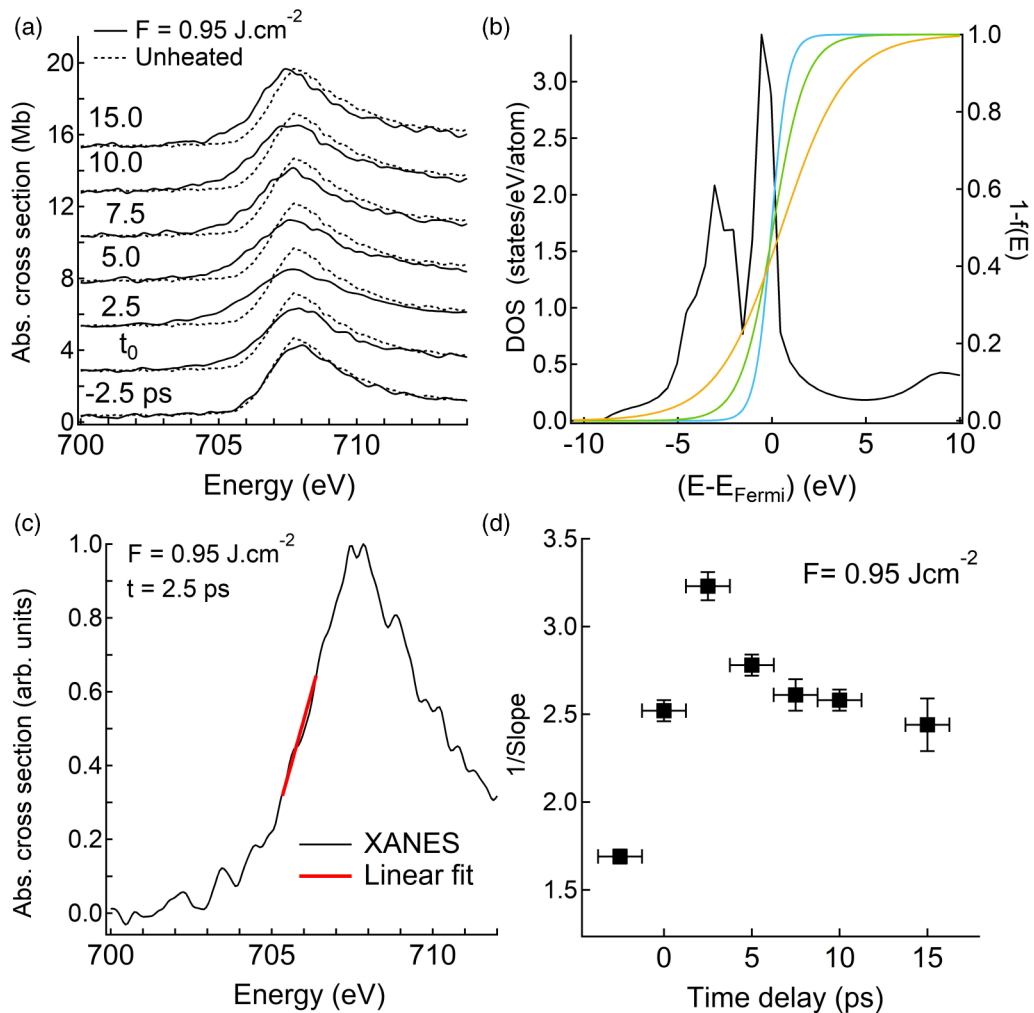
FIG. 2. (a) L_3-edge XANES spectra of iron at selected time delays between the laser pump and the x-ray probe for a fluence $F = 0.95 \, \mathrm{J \, cm^{-2}}$ (solid black lines). For comparison, the unheated spectrum (dotted lines) is also plotted. (b) The DOS at $T_i = 0$ K of bcc iron (left vertical axis) and three Fermi-Dirac distribution curves at 0.1 eV (blue), 0.5 eV (green), and 1 eV (orange) (right vertical axis). (c) A selected XANES spectrum to show the linear fit from which the slope was calculated. (d) Temporal evolution of the $1/s$ curves.

at 707 eV by tuning a broadband x-ray probe pulse of 70 ps duration. According to the dipole selection rules, as the initial state has a p angular momentum, the photoelectron probes the s and d empty states of the DOS, which in Fe are particularly concentrated across the Fermi level [see Fig. 2(b)]. The energy range of the x-ray bandwidth and imaging of the streak camera ($\sim$25 eV) was sufficient to cover the whole XANES region in a single shot. The x-ray spot size was 160 μm (horizontal) $\times$ 100 μm (vertical) to ensure that a relatively uniform heated area was probed within the laser spot. Transmitted x rays were dispersed by a variable-line-spacing (VLS) grating spectrometer [22], which provided about 1 eV energy resolution, and were detected by an x-ray streak camera with a temporal resolution of 2.5 ps [23]. This streak camera detector provides two-dimensional images of the x-ray pulse with time on one axis and photon energy on the other (see Fig. 1).

B. Time-resolved XANES spectra of iron

The L_3-edge XANES spectra of iron at selected time delays between the laser pump and the x-ray probe for a laser

fluence $F = 0.95 \pm 0.04 \, \mathrm{J \, cm^{-2}}$ are shown in Fig. 2(a). They correspond to horizontal lineouts with width corresponding to the 2.5 ps time resolution from the streaked image from Fig. 1. The spectrum at -2.5 ps corresponds to a time delay prior to the arrival of the laser. The laser energy is deposited at t_0 and it represents a sampling of both the unheated ($t < t_0$) and warm dense ($t > t_0$) states, as the laser pulse duration is much shorter than the resolution of the streak camera. For $t > t_0$, several spectral changes are noticeable. The absorption below the edge significantly increases accompanied by a shift to lower energies of about 1.0 eV and the slope of the edge becomes less steep during the first 5 ps following the excitation.

Recent studies on Al [24–27] and Cu [14,15] have demonstrated that XANES is an excellent probe to infer the electron temperature in metals as the slope of the absorption edge is sensitive to smearing of the Fermi surface and thus of the electron temperature since the XANES spectra is essentially the product of the dipole matrix elements (which is sometime approximated by the projected DOS) and the electronic va-

cancy probability $[1 - f(E - E_{Fermi})]$ where $f(E - E_{Fermi})$ is the Fermi-Dirac distribution function [27]. In Fig. 2(b) the electronic density of states of iron (for the solid bcc phase at 0 K) along with several $[1 - f(E - E_{Fermi})]$ vacancy factor curves at three electron temperatures are shown. The Fermi level in iron cuts through the high-energy edge of the $3d$ band. Therefore, moderate electron temperatures can excite $3d$ electrons from below to above the Fermi level. Following the laser pulse absorption, a significant number of unoccupied states are generated which is reflected in the time-resolved XANES spectra by an increase of $2p \rightarrow 3d$ photoabsorption below the L_3 edge. The Fermi-Dirac distribution $f(E - E_{Fermi})$ is an intrinsic function of the electron temperature. The smearing of the slope of the $[1 - f(E - E_{Fermi})]$ curves, and thus of the absorption edge, becomes significant for electron temperatures of the order of 1 eV, as shown in Fig. 2(b). The broadening of the absorption edge in iron is happening in a picosecond timescale that our data is able to resolve. We also observe another change in the XANES spectra, a redshift [28] that we attribute to the laser-induced ultrafast demagnetization effect [29–32]. This phenomenon, the suppression of the magnetic moment by a short laser pulse in ferromagnetic systems, such as iron, has been observed and extensively investigated for more than 20 years [31]. Our DFT electronic structure calculations [17] on bcc iron showed that the Fermi level with a nonmagnetic state was about 0.8 eV lower than with a ferromagnetic state, which is consistent with our experimental observations. The loss of the magnetic moment happens in a subpicosecond timescale and our experimental resolution is not able to resolve its dynamics.

For simple metals like Al, whose DOS behaves as a free electron gas (FEG) and slowly varies with energy, the electron temperature is very linear to the inverse of the slope $(1/s)$ of the K-edge XAS at the inflection point, and T_e can be estimated model free [27]. For warm dense copper, the d bands, which are located a few eV below the Fermi level, are excited into s/p bands and sharp pre-edge features develop in the L_3-edge XAS. As shown in [14] T_e can be estimated by relying on the modeling of the DOS. In the case of iron, the DOS varies significantly at about the Fermi level due to the presence of open shell d bands, hence $1/s$ is likely to deviate from a linear function to the electron temperature [17]. To calculate $1/s$ we have used the following procedure. First, as shown in Fig. 2(c), we normalize the peak height of the experimental spectrum for each time delay to unity and then we calculate the slope s with a linear fit at the normalized spectrum height value 0.5 (FWHM) in an energy range of ± 0.5 eV at E_{FWHM}. Since the absorption spectra were taken as the ratio of the transmitted spectra with and without the target, the systematic uncertainty was canceled out, and the error mainly depends on the noise. Averaging 100 shots reduced the noise level to ~3%. The error bars shown in Fig. 2(c) correspond to the standard deviation of the $1/s$ slope value when varying the energy range across the leading edge of the spectrum instead of the uncertainty derived from a linear fit from a single E range, which would be significantly smaller. We consider that this choice reflects better the sensitivity of the slope to the noise level of the data and to the ambiguity associated to the selection of the E range.

The temporal evolution of $1/s$ of the iron L_3-edge iron for $F = 0.95$ J cm^{-2} is shown in Fig. 2(d). The change in $1/s$ vs time is resolved, reaching a peak value of 3.2 at 2.5 ps, reflecting a higher T_e, and then it is followed by a decay to a value of 2.5 at 15 ps. Experimental data in Fig. 2(d), corroborated by the theoretical predictions discussed in the Introduction, reveal that the energy transfer rate from electron to ions can be significantly slower in warm dense iron (order of several ps) than in weakly photoexcited iron where it exhibits a characteristic relaxation time of 0.25 ps for $T_e \sim 0.1$–0.2 eV [29]. Below we will compare the data with simulations using different models of the thermophysical properties of iron, i.e., the electron-phonon coupling factor, the electronic specific heat and thermal conductivity, to explain such a behavior.

III. THEORETICAL ANALYSIS

A. Two-temperature model simulations

The TTM is widely used to describe the electron-ion equilibration dynamics of a metal irradiated by an ultrashort laser pulse excitation [33]. The evolution of the electron (T_e) and ion (T_i) temperatures are determined by numerically solving the following two coupled heat conduction equations:

$$C_e \frac{\partial T_e}{\partial t} = \frac{\partial}{\partial x}\left(K_e \frac{\partial T_e}{\partial x}\right) - G(T_e - T_i) + S(x, t),$$

$$C_i \frac{\partial T_i}{\partial t} = \frac{\partial}{\partial x}\left(K_i \frac{\partial T_i}{\partial x}\right) + G(T_e - T_i), \qquad (1)$$

where C_e, K_e are the specific heat and thermal conductivity of the electrons and C_i, K_i of the ions. G is the electron-phonon coupling factor. The laser heating source term is modeled as $S(x, t) = \alpha I f(x) g(t)$, where α is the absorption coefficient of the material, I is the incident laser intensity, and $f(x)$ and $g(t)$ are two normalized functions describing the spatial and temporal profile of the laser pulse, respectively. The spatial distribution of the optical excitation exhibits an exponential form $f(x) = \exp[-\frac{z}{\lambda_{OPD}}]$, where λ_{OPD} is the optical penetration depth ($\lambda_{OPD} = 12$ nm for iron), and the temporal profile has a Gaussian form $g(t) = \sqrt{4\ln2/\pi}\exp[-4\ln2(t/t_p)^2]$, where t_p is the laser pulse duration (FWHM). The Debye model, with Debye temperature $\theta_D = 470$ K, is used to calculate C_l. We chose this expression for the spatial distribution of the laser as the measured reflectivity of the laser pulse was close to the room temperature value, which we took as an indication that strong field coupling and nonlinear effects were small.

B. Electron and ion temperature dependence of G and C_e

The electron-phonon coupling factor and the electronic specific heat were calculated by first-principle DFT-MD simulations. A detailed description of these calculations and the theoretical framework used throughout this work can be found in Ref. [17]. The laser fluences used in this work were chosen such that the target would be brought to warm dense matter conditions, where the ion temperature rises from ambient temperature to above 10 000 K in a few picoseconds: physical conditions that are similar to the ones used by Cho *et al.* in Cu, where taking only the electron temperature dependence of G was shown to be insufficient. Accordingly, we investigated not
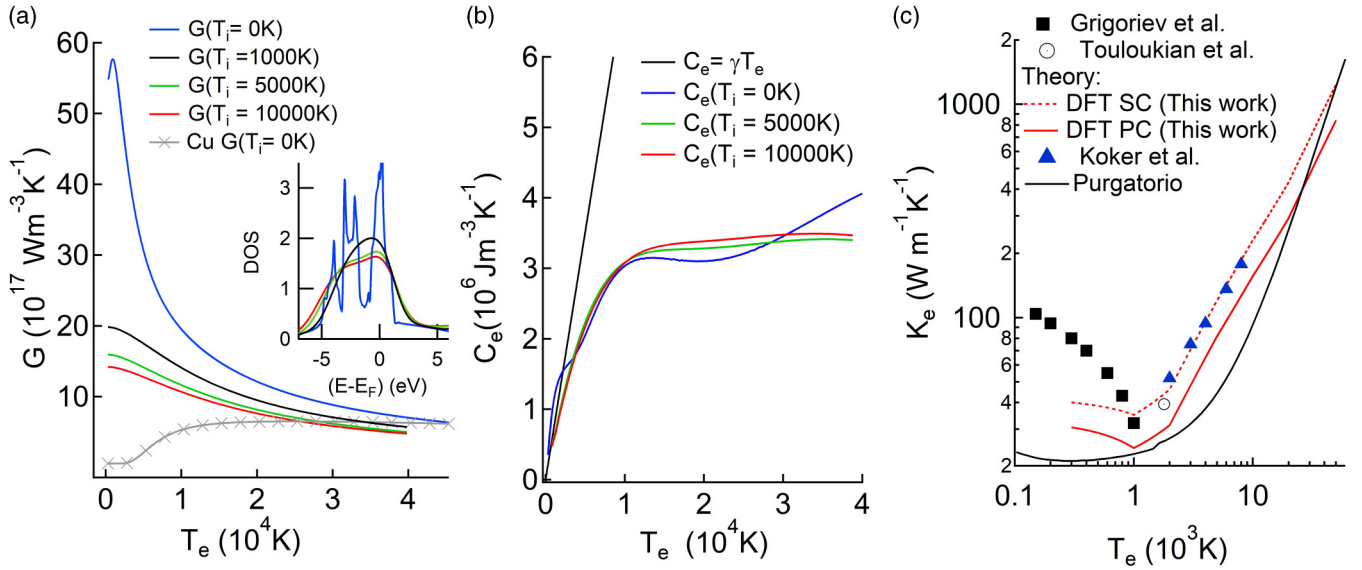
FIG. 3. The electron temperature dependence of (a) the electron-phonon coupling of iron calculated at several ion temperatures (T_i). The blue curve corresponds to $G(T_e)$ with solid DOS at $T_i = 0$ K [6]. This work: black curve corresponds to $G(T_e)$ with fcc solid phase at $T_i = 1000$ K and without spin. The green and red curves correspond to $G(T_e)$ with liquid DOS at a T_i of 5000 and 10 000 K, respectively. The Cu $G(T_e)$ curve at $T_i = 0$ K is shown for comparison [6]. Inset: Iron density of states (DOS) calculated at the same T_i temperatures and colors as for $G(T_e)$ values of Fe. (b) The specific heat of iron calculated at the same ion temperatures as for $G(T_e)$. The black curve corresponds to the specific heat within the FEG approximation. (c) The thermal conductivity of single crystal (red dashed curve) and polycrystalline iron (red solid curve), respectively, estimated in this work from first-principle calculations. Experimental K_e data from [38] at low temperatures are shown as black squares and in the liquid phase with an open circle [39]. Previous *ab initio* calculations are indicated in blue triangles [40] and K_e estimated by Purgatorio, a commonly used plasma-based model [44], is shown as a solid black curve.

only the electron temperature dependence of the DOS but also the ion temperature dependence.

The electron temperature dependence of G is calculated following the formula developed by Wang *et al.* [7] based on the formalism of [34] on the rate of energy exchange between electrons and phonons:

$$G(T_e) = \frac{\pi \hbar k_B \lambda \omega^2}{n(E_f)} \int_{-\infty}^{\infty} n^2(E) \left(\frac{\partial f[(E - \mu)/k_B T_e]}{\partial E} \right) dE,$$

(2)

where $n(E)$ is the DOS, $f(E, \mu, T_e)$ is the Fermi distribution function, μ is the chemical potential for a given T_e, λ is the electron-phonon mass enhancement parameter [35], and $\langle \omega^2 \rangle$ is the second moment of the phonon spectrum defined by McMillan [36]. The $\lambda \langle \omega^2 \rangle$ parameter of iron was estimated from Lin *et al.* $G(T_e)$ calculations and we used the same value for the solid and liquid phases. The ion temperature dependence is taken into consideration when calculating $n(E)$. The Wang formula reflects the few constraints in the original formula. On one hand a transition between electronic states is permitted only from an occupied state to an unoccupied state due to the Pauli exclusion principle and, on the other hand, the energy and momentum conservation laws in an electron-phonon scattering event must be satisfied. One of the goals of this work was to investigate the extent of applicability of the Wang's formula, which in essence, is a high temperature expansion form of the linear perturbation theory where the ion dynamics is described as a harmonic phonon; this approximation is expected to be invalid for hot solid or dense liquid phases. As we shall see, our results are somewhat surprising, and the Wang's formula seems to hold in the warm dense

matter conditions reached in this work. We will discuss this point further after discussing the experimental results.

The electron temperature dependence of the electron-phonon coupling of iron at several ion temperatures below and above the melting temperature are displayed in Fig. 3(a). The first-principle calculations show that the smearing out of the d bands with increasing T_e and T_i has an important impact in the electron-phonon coupling factor. The large G values for $T_e < 10\,000$ K in the $T_i = 0$ K case are reduced by a factor of 3 as T_i reaches 1000 K. Hence, in warm dense iron the electron relaxation dynamics would occur at an appreciably longer timescale than at ambient conditions. Such a behavior is in qualitative agreement with the experimental results shown in Fig. 2(d).

The electron temperature dependence of the electronic specific heat of iron at several ion temperatures is shown in Fig. 3(b). The electronic specific heat $C_e(T_e)$ was calculated by taking the derivative of the total electron energy density with respect to T_e:

$$C_e(T_e) = \int_{-\infty}^{\infty} \frac{\partial f[(E - \mu)/k_B T_e]}{\partial T_e} n(E) E \, dE.$$

(3)

The differences in the calculated $C_e(T_e)$ curves between the solid and liquid DOS are not very pronounced and very small once iron is melted. In contrast, the Sommerfeld approximation $C_e(T_e) = \gamma T_e$ with $\gamma = 702.4$ J m^{-3} K^{-2} [37], which is valid at low temperatures even though often is used beyond condensed matter conditions, significantly diverges for $T_e > 2000$ K from the calculated $C_e(T)$ curves that explicitly take into consideration the DOS of iron.

C. First-principle calculations of the electronic thermal conductivity

The thermal gradient inside the target necessitates inclusion of thermal conduction in the TTM simulations. Thermal conductivity measurements in the WDM regime are challenging and the data are scarce. In Fig. 3(c) we show experimental data from [38] up to 1000 K and in the liquid phase [39], along with the theoretical $K_e(T_e)$ curves from this work calculated from *ab initio* MD calculations up to several tens of thousand of Kelvin and previously reported *ab initio* results [40]. The thermal conductivity was calculated based on the Chester-Thellung-Kubo-Greenwood formula in PAW formula [17]. The PAW approach implemented in VASP was used with the plane wave cutoff energy of 321 eV. We used the Fe_GW 2010 PBE (Perdew-Burke-Ernzerhof) PAW (projector augmented wave) potential from the VASP library. We use the (1/4,1/4,1/4) K point, and the PBE approximation of the exchange-correlation functional. The bcc, fcc, and liquid MD simulations were performed with the simulation box size of 64, 54, and 64 atoms, respectively. Further details of the calculations can be found in Ref. [17]. For thermal conductivity calculations, size effect is known to be relatively large [17]. Thus we used a larger supercell than for G and C_e permissible for a given temperature (up to 250 atoms) in order to assess and correct the size effect. We note that this approach does not use any adjustable or empirical parameters as in other models like Wiedemann-Franz law, where the thermal conductivity is described as the product of electronic conductivity and an empirical parameter. We found that, unlike for G_e and C_e, the nonequilibrium effect is small for K_e once the ion temperature exceeds a few thousand Kelvin. Thus, the $K_e(T_e)$ values used and plotted in Fig. 3(c) were calculated for electron-ion equilibrium conditions (see Ref. [17]). Our results show reasonable agreement with the experimental values near 1000 K, the K_e value in the liquid phase [39], and the previous reported first-principle calculations [40]. At lower temperatures the prediction is less than the experimental values. This is presumably due to lack of accurate lattice phonon contribution in the solid state [41].

The iron targets in this work were polycrystalline not a single crystal. We have estimated the $K_e(T_e)$ of polycrystalline iron using the Mayadas-Shatzkes model for the grain boundary scattering [42,43]:

$$\frac{K_{pc}}{K_{sc}} = 3\left[\frac{1}{3} - \frac{\alpha}{2} + \alpha^2 - \alpha^3 \ln\left(1 + \frac{1}{\alpha}\right)\right]; \quad \alpha = \frac{l}{d}\frac{R}{1-R},$$

(4)

where l is the mean free path of conduction electrons in single crystal material, d is the grain size, and R is the grain boundary reflection coefficient. In our case, $l = 10$ nm, $d = 10$ nm, and $R = 0.25$ [17] were used, which leads to the polycrystalline K_e values being 20% lower than the single-crystal thermal conductivity for $R = 0.25$. Finally, for comparison and completeness, we have also included in Fig. 3(c) the thermal conductivity of iron derived by a commonly used plasma model called Purgatorio which is based on an average-atom calculations model [44]. While Purgatorio and our *ab initio* thermal conductivities agree well each other at high temperature, the Purgatorio value significantly underestimate

K_e at low temperatures, at about $T \sim 1000$ K and lower, compared to both the experimental and *ab initio* data reflecting the nature of approximation used in this model. It is interesting to note that for the temperature range of our interest, from a few thousand to a few tens of thousand Kelvin, the Purgatorio model predicts K_e values significantly lower than the single crystal K_e values calculated by first-principle calculations, however, rather similar to the polycrystalline K_e values.

The precise ion thermal conductivity (K_i) of iron is not known for this temperature range. However, it is expected to be significantly lower than the electronic contribution, and our initial assessment using TTM simulations suggested that the electrons and ions temperature relaxation behavior is less sensitive to K_l than to K_e. In our study, the ion thermal conductivity was chosen to be $K_i/K_e = \sqrt{m_{ele}/m_{Fe}} \sim 1/100$, where m_{Fe} is the atomic mass of iron and m_{ele} is the electron mass. At low temperature, K_l is known to show a maximum below the Debye temperature (θ_D) then rapidly decreases due to exponential increase in the frequency of Umklapp processes [45]. Our TTM analysis indicates, however, that the target temperature exceeds 2000 K in a fraction of a picosecond (0.15 ps), so that underestimation of K_i at low temperature will have a negligible effect on the calculated XANES spectrum after the Gaussian convolution that mimics the experimental detector time resolution of about 2.5 ps.

D. Calculated spatially averaged XANES spectra

As the target had a temperature gradient in the experiments, temperature averaging is necessary for the theoretical XANES calculations. We first calculate the temperature profiles $T_i(x,t)$ and $T_e(x, t)$ using TTM for a given set of thermophysical parameters (G, C_e, K_e). We then perform *ab initio* DFT MD calculations of solid and liquid iron on T_i grid points that covers the maximum range of temperature predicted by the TTM simulations. Using these trajectories, XANES spectrums on the T_i, T_e grid points are calculated as an ensemble average where the electronic structures were relaxed self-consistently for the given T_e. The spatial averaging of the spectra using the TTM derived $T_i(x,t)$ and $T_e(x,t)$ profiles were then performed, where a linear interpolation was used to obtain XANES profile for an arbitrary (T_i, T_e). Lastly we apply a Gaussian time convolution with $\sigma_{FWHM} = 2.5$ ps corresponding to the experimental time resolution. The initial state of the iron target is in a ferromagnetic spin state, and indeed, our XANES calculations were performed for a ferromagnetic state (see details in Ref. [17]). However, the fs-laser pulse suppresses the spin magnetic moment at a subpicosecond timescale, an effect known as ultrafast demagnetization [29–32]. It is therefore important to note that the initial state of the target is modeled as a ferromagnetic state, while the optically excited state should rather be modeled as nonmagnetic, which is the theoretical approach we have taken in this work.

The resultant XANES spectra for selected time delays ($t = 0, 2.5, 5.0$ 10.0 ps) for liquid iron at $T_i = 10\,000$ K together with the one for ambient conditions are shown in Fig. 4(a). Qualitatively, they reproduce all the spectral changes observed in the experimental data [see Fig. 2(a)]. The comparison between an experimental and theoretical XANES spectrum
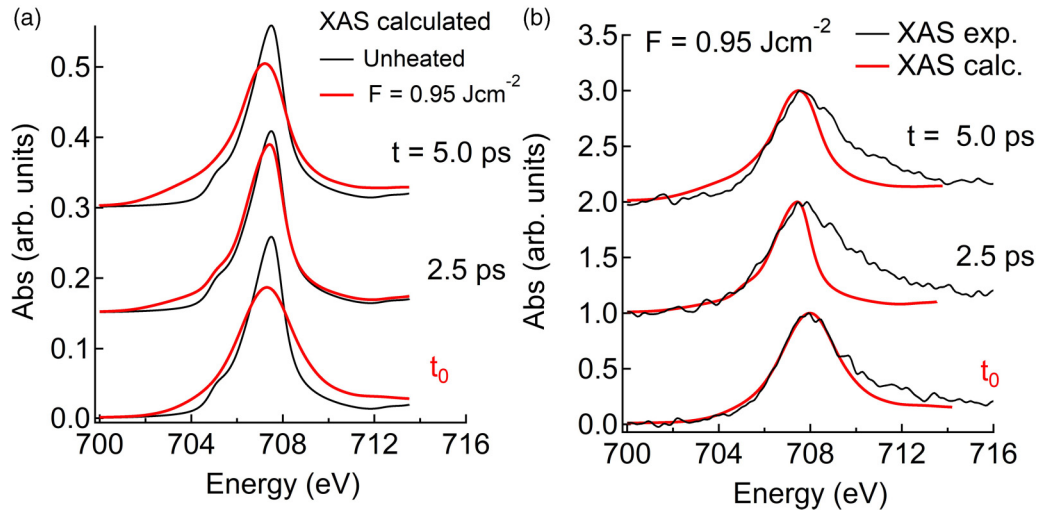
FIG. 4. (a) Spatially average XANES calculated spectra at selected time delays for $T_i = 10\,000$ K and $F = 0.95$ cm^{-2} at selected time delays are shown as solid red lines. The solid black lines correspond to the spectrum at ambient conditions. (b) Comparison between normalized experimental and theoretical XANES spectrum at t_0, 2.5 and 5 ps. Both spectra have been normalized to unity. The theoretical spectra hava been shifted along the energy axis in both graphs to match the energy of the actual L_3 edge for comparison puroposes.

is shown in Fig. 4(b). The theoretical calculated XANES spectrum has a narrower profile than the experimental one. This discrepancy in the width of the spectral shape is observed even at ambient conditions. It is well known that at ambient conditions the XANES calculations based on PBE-GGA (generalized gradient approximation) level calculations give a spectral shape that is narrower than the experimental one, particularly in the high energy side of the spectra.

Interestingly, a similar discrepancy was observed for XANES spectrum calculated at $T = 0$ K using the state-of-art many-body theory, Bethe-Salpeter equation, on ferromagnetic bcc iron [46]. In this case, the disagreement between theory and experiment was attributed to the lack of spin-multiplet effect (spin-orbital coupling), not to many-body correlation effects, which suggests that the similar discrepancy observed in our PBEGGA based XANES spectrum is unlikely to be due to the missing many-body effects [47]. Unfortunately, to the best of our knowledge, there is no *ab initio* XANES calculation code that is able to quantitatively reproduce XANES spectrum of iron in WDM conditions.

IV. COMPARISON BETWEEN CALCULATED AND MEASURED SPECTRAL SLOPE

To overcome these challenges, we have chosen to compare instead an experimental observable that is less affected by the inaccuracy of dipole-matrix elements and is most sensitive to the electron temperature: the inverse of the slope $(1/s)$ at the onset of XANES spectrum. As seen in Fig. 4(b) the slope of the experimental and theoretical spectra shows good agreement within the signal-to-noise level of the experimental spectra.

Figure 5 shows the temporal evolution of the experimental and theoretical $1/s$ curves corresponding to the laser fluence $F = 0.95$ J cm^{-2}. The theoretical $1/s$ curves (solid lines) were calculated for several sets of (G, C_e, K_e) values following the same procedure as for the experimental curves. The com-

parison of $1/s$ starts from $t = 0$ ps not from $t = -2.5$ ps for the following reason. Under ambient conditions at $t < 0$ ps, Fe is in a ferromagnetic state. In this case, the peak corresponding to d states in EDOS for major spin component is pushed down below the Fermi level, while the peak of minor spin components is pushed up above the Fermi level. Accordingly, the inflection point of XANES profile is located above the Fermi level (more than k_BT), and the slope is not related to the electron temperature. As soon as the target is irradiated by the fs laser, ultrafast demagnetization occurs, and ferromagnetism is lost within 1 ps [29,32]. We note that due to the limited time resolution of 2.5 ps in the streak camera, the spectrum at $t = 0(\pm 1.25)$ ps contains spectral contributions from $t < 0$ (before laser excitation) and also $t > 0$ ps (after laser excitation) (see Fig. 2).

In Fig. 5(a) we examine the electron relaxation dynamics for three different models of (G, C_e) with the same thermal conductivity of the polycrystalline K_e case. The FEG model (black solid line), which assumes a constant G (the ambient conditions value 55×10^{17} W m^{-3} K^{-1}) and linear temperature dependence for C_e, is often used at low temperatures. In our high excitation regime, it predicts a much faster decay than the experimental data and an equilibrium temperature much lower due to an overestimation of C_e. Thus, it is clear that this low-temperature model is not appropriate to describe the electron relaxation dynamics of iron in the WDM regime. When $G(T_e)$ and $C_e(T_e)$ calculated for $T_i = 0$ K [6] are used (blue solid line), the predicted $1/s$ curve agrees with the experimental one at later time delays $(t > 7$ ps), when the electrons and the ions are already in equilibrium. However, at earlier time delays, it predicts a much faster relaxation dynamic than the experimental $1/s$ curve reflecting the larger G and it does not reproduce the observed $1/s$ peak value. The same trend was observed when we used the single crystal K_e. So, despite the ambiguity on the K_e absolute values, the dominant thermophysical parameter within the first 5 ps is the G factor [17]. Interestingly, a better agreement is found for
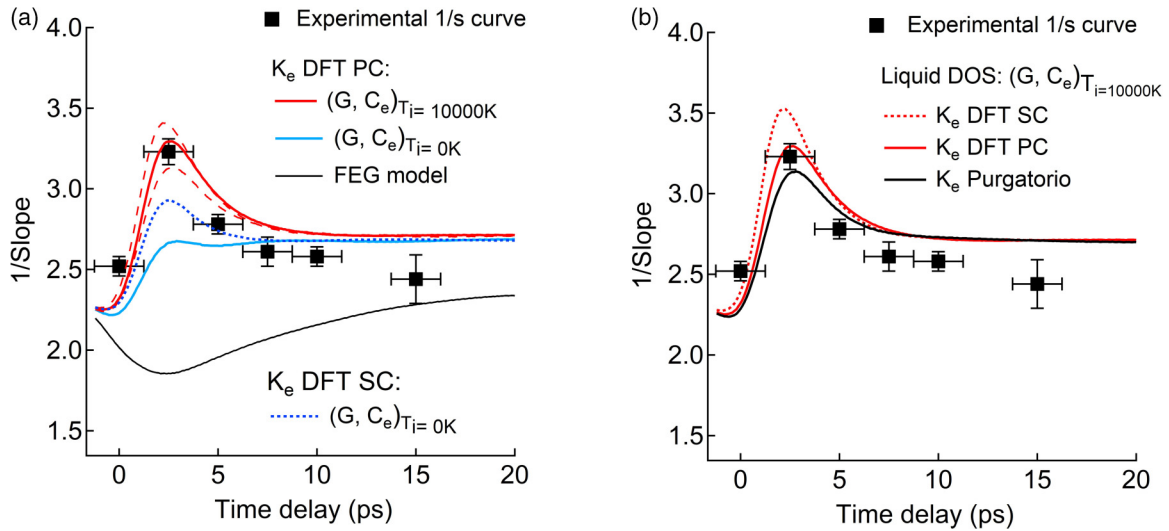
FIG. 5. (a) Comparison of the temporal evolution of $1/s$ curves between the experimental curve (black squares) and several theoretical curves that correspond to the polycrystalline K_e case and three different thermophysical (G, C_e) values: Solid DOS for FEG model (solid black) and lattice temperature at 0 K with Lin's values for (G, C_e) (solid light blue). Liquid DOS for (G, C_e) at $T_i = 10\,000$ K (solid red). The dashed lines correspond to the range of shot-to-shot fluctuations in the laser fluence. (b) Comparison of the temporal evolution of $1/s$ curves between the experimental curve (black squares) and several theoretical curves that correspond to the liquid DOS with an ion temperature of 10 000 K for G and C_e but three different K_e: DFT single crystal (SC) (red dashed curve), DFT with grain scattering for polycrystalline Fe (PC) (solid red), and the plasma-based model Purgatorio (solid black).

$G(T_e)$ and $C_e(T_e)$ calculated using a liquid DOS with $T_i = 10\,000$ K (red solid line). This new calculation reproduces the measured peak $1/s$ value as well as the decay rate. The value $T_i = 10\,000$ K was chosen from the spatially average equilibration temperature from our TTM calculations at the laser fluence of $0.95\,\mathrm{J\,cm^{-2}}$. These results provide evidence that T_i dependence needs to be considered to calculate G in WDM. At later time delays ($t > 10$ ps) the experimental $1/s$ curve decays faster than the model-based curves, indicating the onset of other cooling mechanisms and possible expansion of the target. Figure 5(b) shows the sensitivity to the different K_e models with (G, C_e) calculated at $T_i = 10\,000$ K. The $1/s$ curves corresponding to the polycrystalline and Purgatorio model lay within the experimental accuracy, whereas the single crystal $K_e(T_e)$ curve is outside the error bars at the peak of $1/s$. More detailed comparisons on the G, C_e dependence and T_i effects on $1/s$ can be found in Ref. [17]. We note that the naming of single/polycrystal may be misleading above the melting temperature and another nomenclature like bulk liquid could have been used. However, the term bulk does not discriminate between single or polycrystal within the solid state. The treatment presented here is the first attempt to take into account the thermal conductivity contribution in the electron-phonon relaxation dynamics and it should be taken as an approximation. Its validity needs to be examined more thoroughly in the future when experimental data are available.

V. DISCUSSION

In this study TTM simulations with full T_e, T_i dependence were not performed due to computational limitations. Therefore, the comparison of the simulated $1/s$ shown in Fig. 5 with the experimental $1/s$ curve is not intended to determine the

set of G and C_e in a truly quantitative manner yet. However, our observations on $1/s$ profiles clearly indicate significant reduction of G value of iron in WDM conditions and the importance of including T_i dependency in describing thermophysical properties. In order to demonstrate these points, we have made a simplified analysis on the temperature relaxation timescale as follows.

The spatial distribution of the electron and ion temperatures within the target thickness at selected time delays are shown in Figs. 6(a) and 6(b), respectively. These temperature profiles where obtained by solving the TTM at the experimental fluence value of $0.95\,\mathrm{J\,cm^{-2}}$ and using the set of thermophysical values (G, C_e, and K_e) that have shown good agreement with the experimental $1/s$ curves. These profiles show the temperature gradient and temperature range achieved within the iron target. The majority of the target reaches electron and ion temperatures within the WDM regime. In Fig. 6(c) the temporal evolution of the spatially averaged T_e is shown. $T_e(t)$ reaches a peak value of about 19 000 K very rapidly and then decayes to a value close to 10 000 K. The $T_e(t)$ decay profile was fitted to the following exponential function $f(t) = A\exp(\frac{-t}{\tau_{\mathrm{rel}}}) + B$, $t > 0$, with the resulting fitting parameter values: $A = 9150 \pm 32$ K, $B = 11870 \pm 36$ K, and the characteristic electron-phonon relaxation time of $\tau_{\mathrm{rel}} = 2.6 \pm 0.1$ ps. At lower temperatures (e.g., 1000 K), τ_{rel} is reported to be about 0.25 ps [29] which would imply an electron relaxation about ten times faster than in our experiments. We have also performed a similar exponential decay fit to the calculated $1/s$ profile, calculated at the same thermophysical values and a Gaussian convolution of 0.15 ps instead of the experimental resolution of 2.5 ps. The electron-phonon relaxation time obtained from the fit is 2.0 ± 0.1 ps. The two relaxation constants are quite consistent and given that the averaging process to obtain the $1/s$ profile from
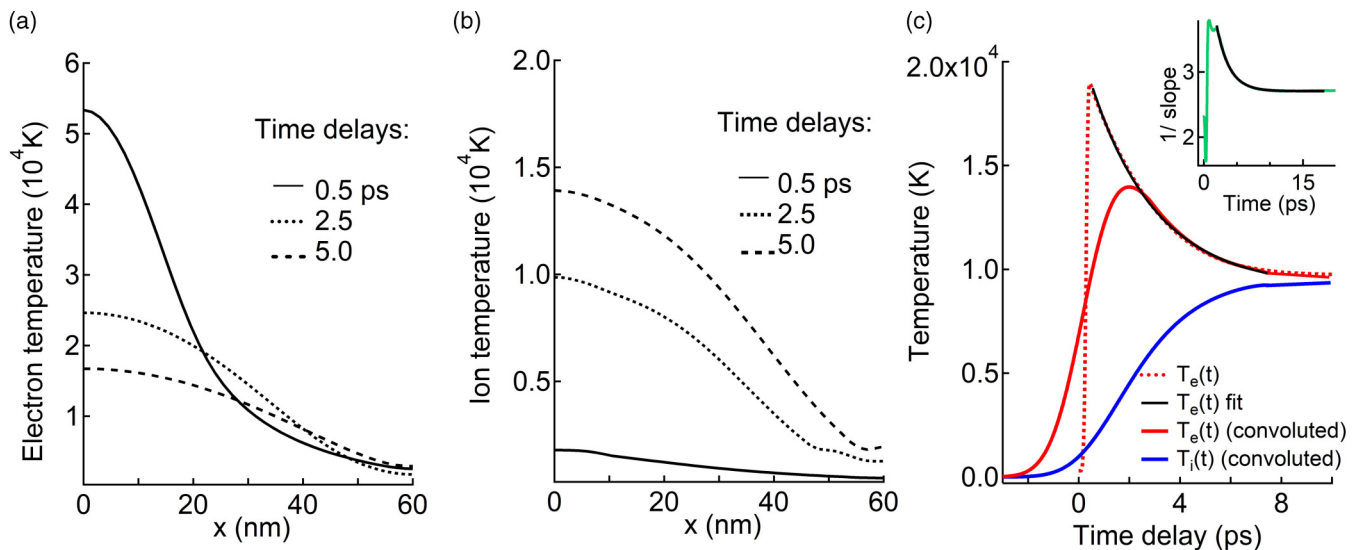
FIG. 6. Spatial distribution of the electron (a) and ion (b) temperatures at selected time delays $t = 0.5$, 2.5, and 5.0 ps. The profiles were calculated by solving the TTM at the same fluence as the experimental data $F = 0.95 \, \mathrm{J \, cm^{-2}}$ and using the following set of thermophysical parameters: Liquid DOS for (G, C_e) at $T_i = 10\,000$ K and K_e with grain scattering for polycrystalline Fe (PC). (c) Time evolution of the spatially average T_e (dotted red line), 2.5 ps Gaussian convoluted $T_e(t)$ (solid red line), and $T_i(t)$ (solid blue line) curves and the exponential decay fit to the unconvoluted $T_e(t)$ curve (black solid line). Inset: Temporal evolution of the calculated $1/s$ curve corresponding to the same thermophysical parameters with a Gaussian time convolution of 0.15 ps (green curve). Exponential decay fit (solid black line) of the $1/s$ profile.

the calculated XANES spectra is a highly nonlinear process, it is not surprising that the values differ slightly. All these results are clear evidences that the electron-phonon coupling of iron in WDM condition is significantly reduced, which is consistent with the theoretical prediction based on the Wang's formula [6].

In this work, due to the limitations in the laser system and the experimental configuration, higher fluences were not achievable. As such, and by chance, the characteristic relaxation time of WD Fe and the experimental time resolution of the streak camera are very similar. This is the reason why our $1/s$ curves do not resolve the sharp rise and true peak of $T_e(t)$. This is reflected in Fig. 6(c), where the temporal evolution of the spatially average electron temperature convolved with the 2.5 ps time resolution is plotted. The sharp peak in the $T_e(t)$ profile is now much lower and wider, and thus, less pronounced. These features are similar to what we observe in the $1/s$ profiles. This issue could be mitigated in the future by probing the nonequilibrium dynamics of WD Fe at a higher photoexcitation, which would lead to longer relaxation timescales, or use a different diagnostic and experimental setup with a shorter time resolution.

The theories of electron-ion coupling in condensed matter and in plasma conditions are currently disconnected, and our intention was to bridge these two regimes in a seamless fashion. The essence of the Wang's approximation originates in the temperature scale of WDM (eV) that is significantly larger than the Debye temperature, which results in having electron temperature dependency via EDOS and the Fermi occupation [7], and details of the phonon properties are completely omitted except for the Debye temperature that represents the energy scale of ion fluctuation. Electron-ion coupling in plasma conditions are often described as the interaction between charged particles and current induced by

the density fluctuation of opposite charge particles, where the term corresponding to the current induced by positive ions is usually omitted for the same reasons as in the condensed matter approach. The approximation stems from the mass difference between electrons and nucleis. Interestingly, in the quantum mechanical description of G based on the Fermi golden rule, the electron fluctuation is described based on the free electron EDOS which is a commonly used approximation in plasma physics that is well justified if the energy scale of the fluctuation is significantly larger than the electronic shell structure [48,49]. Otherwise, these two formulas from condensed matter physics and plasma physics share the same basic structure: a scale prefactor multiplied by the electron temperature dependent term consisting of EDOS. In WDM conditions, the relevant energy scale is about electron volts where significant change in EDOS takes place, and is reflected in the predicted G behavior of metals [6]. In such conditions, the use of a free electron EDOS is unlikely to be justified. We speculate that the smaller energy scale of the ion fluctuation compare to that of the electron fluctuation may have led to the seemingly success of the Wang's G formula so far. However, we note that further investigation on this issue is needed given the highly approximative nature of the theoretical treatment [6,7,14,17]. So far experimental evidences that are consistent with this picture have been presented for Au, Cu, Al [7–15], and we have successfully provided the evidence for Fe in this study. In order to optimize the sensitivity of the XANES technique to the electron temperature, a K-edge spectroscopy could be carried out to minimize the sensitivity of the technique to drastic d-DOS changes (as an effect of the dipole selection rules) occurring across the Fermi level. XANES measurements at Fe K edge would require a hard x-ray source and a high-resolution spectrometer, which could be possible at other facilities.

VI. SUMMARY

We have measured the time-resolved XANES spectra of a fs-laser-heated iron foil at $0.95 \, \mathrm{J \, cm^{-2}}$ and developed a novel analysis for nonhomogeneous heating conditions. One of the goals of this study was to examine the validity of Wang's formula for the G coupling calculations in transition metals. Our results suggest that Wang's formula is valid up to the temperature range explored in our experiments, a few electron volts, wherein significant reduction of G at elevated temperature was predicted for iron resulting in a significant slowdown of the energy transfer from the hot electrons to the lattice: an order of magnitude difference between condensed matter and WDM conditions. Our analysis indicates that the ion temperature dependence of G is significant for iron in WDM conditions, which is consistent with the previous report on Cu by Cho *et al.* We have presented a combined theory-experimental approach that can assess with great sensitivity to the thermophysical parameters in nonequilibrium WDM

conditions. Furthermore, future experiments could employ targets with varying thickness to maximize the sensitivity to the thermophysical properties based on which, the validity of various theoretical models of thermophysical properties including hot liquid models [48,49] and the Wang's formula can be evaluated quantitatively for a wider range of physical conditions, which will help to establish our understanding of the electron-ion nonequilibrium equilibration in WDM physics.

[1] R. W. Lee, H. A. Baldis, R. C. Cauble, O. L. Landen, J. S. Wark, A. Ng, S. J. Rose, C. Lewis, D. Riley, J.-C. Gauthier, and P. Audebert, Laser Part. Beams **20**, 527 (2002).

[2] H. J. Lee, P. Neumayer, J. Castor, T. Döppner, R. W. Falcone, C. Fortmann, B. A. Hammel, A. L. Kritchner, O. L. Landen, R. W. Lee *et al.*, Phys. Rev. Lett. **102**, 115001 (2009).

[3] M. Ross, Nature (London) **292**, 435 (1981).

[4] T. R. Dittrich, S. W. Haan, M. M. Marinak, S. M. Pollaine, D. E. Hinkel, D. H. Munro, C. P. Verdon, G. L. Strobel, R. McEachern *et al.*, Phys. Plasmas **6**, 2164 (1999).

[5] J. W. Chan, T. Huser, S. Risbud, and D. M. Krol, Opt. Lett. **26**, 1726 (2001).

[6] Z. Lin, L. V. Zhigilei, and V. Celli, Phys. Rev. B **77**, 075133 (2008), The iron data are not included in the paper but at this website: http://www.faculty.virginia.edu/CompMat/electron-phonon-coupling/.

[7] X. Y. Wang, D. M. Riffe, Y.-S. Lee, and M. C. Downer, Phys. Rev. B **50**, 8016 (1994).

[8] J. Hohlfeld, S.-S. Wellershoff, J. Güdde, U. Conrad, V. Jähnke, and E. Matthias, Chem. Phys. **251**, 237 (2000).

[9] T. Ao, Y. Ping, K. Widmann, D. F. Price, E. Lee, H. Tam, P. T. Springer, and A. Ng, Phys. Rev. Lett. **96**, 055001 (2006).

[10] Y. Ping, D. Hanson, I. Koslow, T. Ogitsu, D. Prendergast, E. Shcwegler, G. Collins, and A. Ng, Phys. Rev. Lett. **96**, 255003 (2006).

[11] R. Ernstorfer, M. Harb, C. T. Hebeisen, G. Sciaini, T. Dartigalongue, and R. J. D. Miller, Science **323**, 1033 (2009).

[12] J. Chen, W.-K. Chen, J. Tang, and P. M. Rentzepis, Proc. Natl. Acad. Sci. USA **108**, 18887 (2011).

[13] Z. Chen, B. Holst, S. E. Kirkwood, V. Sametoglu, M. Reid, Y. Y. Tsui, V. Recoules, and A. Ng, Phys. Rev. Lett. **110**, 135001 (2013).

[14] B. I. Cho, K. Engelhorn, A. A. Correa, T. Ogitsu, C. P. Weber, H. J. Lee, J. Feng, P. A. Ni, Y. Ping, A. J. Nelson, D. Prendergast, R. W. Lee, R. W. Falcone, and P. A. Heimann, Phys. Rev. Lett. **106**, 167601 (2011).

[15] B. I. Cho, T. Ogitsu, K. Engelhorn, A. A. Correa, Y. Ping, J. W. Lee, L. J. Bae, D. Prendergast, R. W. Falcone, and P. A. Heimann, Sci. Rep. **6**, 18843 (2016).

[16] H. E. Elsayed-Ali, T. B. Norris, M. A. Pessot, and G. A. Mourou, Phys. Rev. Lett. **58**, 1212 (1987).

[17] T. Ogitsu, A. Fernandez-Pañella, S. Hamel, A. A. Correa, D. Prendergast, C. D. Pemmaraju, and Y. Ping, Phys. Rev. B **97**, 214203 (2018).

[18] K. Engelhorn, V. Recoules, B. I. Cho, B. Barbrel, S. Mazevet, D. M. Krol, R. W. Falcone, and P. A. Heimann, Phys. Rev. B **91**, 214305 (2015).

[19] P. B. Johnson and R. W. Christy, Phys. Rev. B **9**, 5056 (1974).

[20] D. R. Lide, *CRC Handbook of Chemistry and Physics*, 82nd ed. (CRC, Boca Raton, FL, 2001).

[21] J. Hohlfeld, J. G. Müller, S.-S. Wellershoff, and E. Matthias, Appl. Phys. B **64**, 387 (1997).

[22] P. Heimann, T. E. Glover, D. Plate, H. J. Lee, V. C. Brown, H. A. Padmore, and R. W. Schoenlein, AIP Conf. Proc. **879**, 1195 (2007).

[23] J. Feng, K. Engelhorn, B. I. Cho, H. J. Lee, M. Greaves, C. P. Weber, R. W. Falcone, H. A. Padmore, and P. A. Heimann, Appl. Phys. Lett. **96**, 134102 (2010).

[24] K. Oguri, Y. Okano, T. Nishikawa, and H. Nakano, Phys. Rev. Lett. **99**, 165003 (2007).

[25] A. Mančić, A. Lévy, M. Harmand, M. Nakatsutsumi, P. Antici, P. Audebert, P. Combis, S. Fourmaux, S. mazevet, O. Peyrusse, V. Recoules, P. Renaudin, J. Robiche, F. Dorchies, and J. Fuchs, Phys. Rev. Lett. **104**, 035002 (2010).

[26] P. M. Leguay, A. Lévy, B. Chimier, F. Deneuville, D. Descamps, C. Fourment, C. Goyon, S. Hulin, S. Petit, O. Peyrusse, J. J. Santos, P. Combis, B. Holst, V. Recoules, P. Renaudin, L. Videau, and F. Dorchies, Phys. Rev. Lett. **111**, 245004 (2013).

[27] F. Dorchies, F. Festa, V. Recoules, O. Peyrusse, A. Benuzzi-Mounaix, E. Brambrink, A. Lévy, A. Ravasio, M. Koenig, T. Hall, and S. Mazevet, Phys. Rev. B **92**, 085117 (2015).

[28] E. Principi, E. Giangrisostomi, R. Mincigrucci, M. Beye, G. Kurdi, R. Cucini, A. Gessini, F. Bencivenga,

and C. Masciovecchio, Phys. Rev. B **97**, 174107 (2018).

[29] E. Carpene, E. Mancini, C. Dallera, M. Brenna, E. Puppin, and S. De Silvestri, Phys. Rev. B **78**, 174422 (2008).

[30] J. Hohlfeld, E. Matthias, R. Knorren, and K. H. Bennemann, Phys. Rev. Lett. **78**, 4861 (1997).

[31] E. Beaurepaire, J. C. Merle, A. Daunois, and J. Y. Bigot, Phys. Rev. Lett. **76**, 4250 (1996).

[32] A. Fognini, T. U. Michimayr, G. Salvatella, C. Wetly, U. Ramsperger, T. Bähler, F. Sorgenfrei, M. Beye, A. Eschenlohr *et al.*, Appl. Phys. Lett. **104**, 032402 (2014).

[33] S. I. Anisimov, B. L. Kapeliovich, and T. L. Perel'man, Zh. Eksp. Teor. Fiz. **66**, 776 (1974) [JETP **39**, 375 (1974)].

[34] P. B. Allen, Phys. Rev. Lett. **59**, 1460 (1987).

[35] G. Grimvall and E. Wohlfarth, *Selected Topics in Solid State Physics* (North-Holland, New York,1981).

[36] W. L. McMillan, Phys. Rev. **167**, 331 (1968).

[37] C. Kittel, *Introduction to Solid State Physics*, 8th ed. (Wiley, New York, 2004).

[38] I. S. Grigoriev and E. Z. Meilikhov, *Handbook of Physical Quantities* (CRC Press, Boca Raton, FL, 1997).

[39] Y. S. Touloukian, R. W. Powell, C. Y. Ho, and P. G. Klemens, *Thermal Conductivity-Metal Elements and Alloys* (IFI/Plenum, New York, 1971).

[40] N. de Koker, G. Steinle-Neumann, and V. Vlček, Proc. Natl. Acad. Sci. USA **109**, 4070 (2012).

[41] G. D. Mahan, Phys. Rev. **163**, 612 (1967).

[42] A. F. Mayadas and M. Shatzkes, Phys. Rev. B **1**, 1382 (1970).

[43] A. F. Mayadas, M. Shatzkes, and J. F. Janak, Appl. Phys. Lett. **14**, 345 (1969).

[44] B. Wilson, V. Sonnad, P. Sterne, and W. Isaacs, J. Quant. Spectrosc. Radiat. Transfer **99**, 658 (2006).

[45] B. Koopmans, M. van Kampen, J. T. Kohlhepp, and W. J. M. de Jonge, Phys. Rev. Lett. **85**, 844 (2000).

[46] J. Vinson, Bethe-Salpeter Equation Approach for Calculations of X-ray Spectra, Ph.D. thesis, University of Washington, 2012.

[47] C. J. Cramer and D. G. Truhlar, Phys. Chem. Chem. Phys. **11**, 10757 (2009).

[48] D. A. Chapman, J. Vorberger, and D. O. Gericke, Phys. Rev. E **88**, 013102 (2013).

[49] G. Hazak, Z. Zinamon, Y. Rosenfeld, and M. W. C. Dharma-Wardana, Phys. Rev. E **64**, 066411 (2001).